Dalton Transactions

ROYAL SOCIETY OF CHEMISTRY

PAPER

View Article Online
View Journal

Cite this: DOI: 10.1039/d5dt02825f

A copper phosphide electrocatalyst enables high-areal-capacity and long-term stability in lithium–sulfur pouch cells

Sooan Bae,†[a,b,c] Jihyeon Park, †[a,b,c] Laurin Rademacher,[d] Songhyun Lee,[a] Chaehyeong Lee,[a,b,c] Vivek Bharatbhai Kathiriyam,[d] Maryam Nojabaee, [d] Andreas Friedrich, [d] Jaeyoung Lee *[a,b,c] and Jin Won Kim*[a,b,c]

Despite their high theoretical energy density, the commercial viability of lithium–sulfur batteries (LSBs) is impeded by issues of poor sustainability, primarily stemming from the shuttle effect of lithium polysulfides. To address this challenge, we have developed a novel copper phosphide (CuP_2) electrocatalyst. Through ball-milling, CuP_2 is synthesized with copper- and oxide-based catalytic surface active sites that demonstrate strong adsorption of lithium polysulfides. This enhanced adsorption effectively suppresses the shuttle effect, leading to significant improvements in battery lifespan and initial capacity. By optimizing the CuP_2 content in the interlayer to 10 wt%, enhanced cell reversibility is achieved. A coin cell fabricated with the optimized interlayer delivers an initial capacity of 964 mAh g^{-1} and maintains a robust capacity of 600 mAh g^{-1} after 500 cycles at a 0.5 C rate. Critically, the practical applicability of this approach is confirmed in a pouch cell, where the areal capacity is doubled to 2.2 mAh cm^{-2} with the inclusion of the CuP_2 catalyst. This work, therefore, presents a new avenue for the rational design of highly efficient electrocatalysts for next-generation LSBs.

Received 25th November 2025,
Accepted 14th January 2026

DOI: 10.1039/d5dt02825f

rsc.li/dalton

1. Introduction

The global climate crisis has produced numerous challenges, one of which currently involves shifting from fossil fuel-dependent energy systems to renewable energy systems.[1] In the development of new rechargeable battery technologies for small electronics and electric vehicles, fast response times and high capacities are required, which must exceed those of lithium-ion batteries (LIBs). As a result, lithium–sulfur batteries (LSBs) have received growing attention as lighter and longer-lasting batteries owing to their high theoretical gravimetric energy densities,[2–4] which are typically five-fold higher than those of LIBs.[5,6] In addition, the sulfur active material present in LSBs is both abundant and cheap.

However, LSBs tend to exhibit poor long-term performance due to the polysulfide shuttle effect.[7] This phenomenon involves the diffusion of intermediate liquid-phase lithium polysulfides (LiPSs, Li_2S_x, $3 < x < 8$) from the cathode into the remainder of the cell.[8] This causes side reactions on the Li metal surface, resulting in self-discharge or passivation, along with a corresponding increase in the cell resistance owing to electrolyte contamination by the eluted LiPSs.[4,9–12] Furthermore, the eluted LiPS are randomly redeposited within the porous cathode matrix, resulting in irreversible active material losses, blockage of the Li-ion pathways, and an accelerated performance degradation.

A primary challenge in LSB development is the notorious "shuttle effect" of LiPS, which leads to rapid capacity decay. Initial attempts to solve this involved physical confinement, using materials like porous carbon to trap sulfur within the cathode.[13–20] However, this method offers limited control over soluble LiPS intermediates. A more effective strategy is chemisorption, which employs catalysts to anchor LiPS and accelerate their conversion kinetics. The pursuit of highly active electrocatalysts to mediate the LiPS conversion process remains a central focus in the field, and a number of recent studies have demonstrated significant progress by employing advanced catalytic materials to immobilize polysulfides and accelerate their reaction kinetics effectively.[21–24] While various metal

[a]Department of Environment and Energy Engineering, Gwangju Institute of Science and Technology (GIST), 123 Cheomdangwagi-ro, Gwangju, 61005, Republic of Korea. E-mail: jaeyoung@ gist.ac.kr, lukeyiruma@gmail.com
[b]International Future Research Center of Chemical Energy Storage and Conversion Processes, GIST, 123 Cheomdangwagi-ro, Gwangju, 61005, Republic of Korea
[c]ERTL Center for Electrochemical and Catalysis, GIST, 123 Cheomdangwagi-ro, Gwangju, 61005, Republic of Korea
[d]Institute of Engineering Thermodynamics, German Aerospace Center (DLR), Pfaffenwaldring 38-40, Stuttgart, 70569, Germany
† Co-first author: These authors contributed equally to this work.

oxides (*e.g.*, Al_2O_3, TiO_2, Co_3O_4, NiO, and CoC_2O_4) have been investigated for this purpose, a well-documented challenge is their inherently poor electrical conductivity.[25–32] These materials are typically semiconducting or insulating, which creates a significant performance bottleneck by hindering the rapid electron transfer required for efficient polysulfide redox reactions.[33,34] This critical trade-off between catalytic activity and electrical conductivity necessitates the exploration of new material cases. Our previous work demonstrated that metal phosphides, and specifically CuP_2, are highly active electrocatalysts for the multi-step CO_2 reduction reaction.[35] Given their superior conductivity compared to oxides, we identified CuP_2 as a promising candidate to overcome the limitations of conventional catalysts and effectively enhance the electrochemical performance of LSBs.

The rational design of catalysts for LSBs can be guided by principles drawn from analogous electrochemical systems. In this work, we establish a conceptual link between Li–S chemistry and CO_2 electroreduction based on two key parallels. First, both systems involve complex, multi-electron redox cascades with soluble intermediates, where catalyst performance depends on effectively managing these species. Second, from a fundamental chemical perspective, sulfur and oxygen exhibit similar behaviors, notably their high electronegativity and propensity to form reactive anions (polysulfides and oxyanions, respectively). Based on this framework, we posit that catalysts proficient in mediating reactions involving oxygen species could be successfully repurposed to regulate polysulfide conversion. Inspired by our prior success in demonstrating CuP_2 as a highly active catalyst for CO_2 conversion, we investigate its application in LSBs. The central aim of this study is to validate that the catalytic properties of CuP_2 can be leveraged to enhance LiPS retention and improve the electrochemical performance of LSBs.

2. Experimental

To synthesize CuP_2 catalysts, $CuCl_2$ and red phosphorus (>99%, Alfa Aesar) were mixed in a 1 : 2 molar ratio and ball-milled with zirconia balls at 600 rpm in an Ar atmosphere. The CuP_2-coated separator, serving as an interlayer, was formulated by mixing Super-P and vapor-grown carbon fibers (VGCF-H) with *N*-methyl-2-pyrrolidone (NMP) in a weight ratio of 15 : 55 : 30. The obtained slurry was coated onto a Celgard 2320 separator *via* vacuum filtration, and the coated separator was dried in a vacuum oven at 60 °C for 24 h. After this time, the dried separator was punched into 16.0 mm diameter disks with a thickness of *ca.* 20 μm.

The crystal phase of the as-prepared sample was analyzed by X-ray diffraction (XRD, Miniflex II, Rigaku) with Cu Ka radiation (λ = 0.15406 nm). The morphology of the sample before the battery cycling was characterized using scanning electron microscopy (SEM, S-4700, Hitachi) and transmission electron microscopy (TEM, F200X, Talos). In addition, energy-dispersive X-ray spectroscopic (EDS) mapping was simultaneously conducted to determine the elemental composition of the Li anode. X-ray photoelectron spectroscopy (XPS) was used to analyze the binding energies of the surface elements before and after the LiPS adsorption tests.

A 0.2 M Li_2S_6 solution was prepared by dissolving elemental sulfur and Li_2S (5 : 1 molar ratio) in a 1 : 1 (v/v) mixture of 1,3-dioxolane (DOL) and 1,2-dimethoxyethane (DME). For the adsorption test, the CuP_2 catalyst powder was added to the Li_2S_6 solution, and a color change was observed after allowing the mixture to settle for more than 3 h. The amount of residual polysulfide was determined by ultraviolet-visible (UV-vis) spectroscopy based on the absorption change at *ca.* 268 nm. After removal of the supernatant, the remaining solid was analyzed by XPS to examine the interactions between the LiPSs and the CuP_2 catalyst.

The cathode was prepared by mixing a sulfur/carbon composite, conductive Super-P, and a CMC/PEO binder with a weight ratio of 80 : 10 : 10. For the sulfur/carbon composite, elemental sulfur was initially mixed with Ketjen black (EC600JD, Lion Specialty Chemicals) in a 7 : 3 ratio, and ball-milled under an argon atmosphere at 500 rpm for 15 min, followed by sufficient cooling. The sulfur content of the composite was confirmed to be *ca.* 70% using thermogravimetric analysis (TGA). A slurry was prepared by vigorously mixing the solid powder (maintained at the aforementioned 80 : 10 : 10) with deionized water to achieve a final solids content of 25 wt%. The slurry was coated onto a carbon-coated foil using a doctor blade and dried at 60 °C in a vacuum oven for 1 day, resulting in sulfur loading ranging from 1.0 to 1.5 mg cm^{-2}.

To compare the blank and CuP_2-coated separators, electrochemical measurements were performed using 2032-coin cells assembled in an Ar-filled glove box (<0.5 ppm H_2O). The cells were assembled by stacking two electrodes and a separator with the electrolyte. To observe the electrochemical reaction over the CuP_2 catalyst, cyclic voltammetry (CV) and cycling tests were conducted using a WBSC 300 cycler (Won-A Tech). The CV measurements were performed at a scan rate of 0.1 mV s^{-1} in the 1.5–3.0 V *vs.* Li/Li^+ potential window to evaluate the catalytic effect of CuP_2. All data were recorded after sufficient activation to allow the cathode containing a higher sulfur loading to undergo efficient wetting. Cycling tests were carried out at various current densities to assess the cell capacity and stability. To further investigate the adsorption capacity of CuP_2, the surface of the Li anode was analyzed using SEM-EDS to quantify the presence of sulfur after repeated cycling. Electrochemical impedance spectroscopy (EIS) was performed at the open-circuit voltage (OCV) using a Bio-Logic potentiostat (NEO Science) over a 4–60 MHz frequency range to investigate the role of CuP_2 as a redox mediator. Finally, long-term cycling tests were conducted at a 0.2 C rate to evaluate the overall cell performance and stability.

For pouch-cell fabrication, conventional sulfur cathodes (3 cm × 5 cm), both with and without a CuP_2 interlayer, were stacked with an anode (3.2 cm × 5.2 cm) and a separator (Celgard C2500). A Li metal foil (MSE Supplies) with a thickness of 500 μm was used as the anode. The electrolyte was

composed of 1 M lithium bis(trifluoromethanesulfonyl)imide (LiTFSI, Sigma-Aldrich) and 0.5 M $LiNO_3$ (Sigma-Aldrich) dissolved in a 1 : 1 (v/v) 1,3-dioxolane (DOL, Thermo Scientific)/ethylene glycol dimethyl ether (DME, Thermo Scientific) solution. The cycling test of the pouch cell was conducted using a galvanostatic method with a cutoff voltage range of 1.9–2.6 V. Before the test, the assembled cell underwent a 5 hour rest period as part of the pre-activation process. The initial cycle was performed at a discharge rate of 0.05 C and a charge rate of 0.1 C, while subsequent cycles were conducted at a consistent rate of 0.1 C for both discharge and charge. Cycling was performed using Basytec: CTS Lab with 16 Channels and CTS Standard with 32 Channels.

3. Results and discussion

The structure and morphology of the synthesized CuP_2 catalyst were investigated, with the results presented in Fig. 1. First, the crystallinity and phase purity were confirmed by XRD. As shown in Fig. 1a, all diffraction peaks for the as-prepared powder are in excellent agreement with the standard pattern for crystalline CuP_2 (JCPDS No. 01-076-1190). The morphology of the catalyst was then examined using electron microscopy. The SEM image in Fig. 1b shows that the powder forms irregular clusters 2–3 μm in size. TEM analysis reveals that these clusters are composed of primary nanoparticles with an average diameter of 4–5 nm (Fig. 1c). Finally, the catalyst was coated onto a separator to form a functional interlayer. The cross-sectional SEM image in Fig. 1d confirms a uniform coating with a thickness of *ca.* 20 μm. Corresponding EDS mapping for copper (Fig. 1e) and phosphorus (Fig. 1f) demonstrates a homogeneous elemental distribution, verifying a high-quality and uniform catalyst coating.

To probe the electrocatalytic effect of the synthesized CuP_2 interlayer on the redox kinetics of LiPS, CV was performed. As shown in Fig. 2a, both the blank cell and the cell with the CuP_2 interlayer exhibit the characteristic redox peaks of a lithium–sulfur battery: two cathodic peaks for the reduction of sulfur to high-order (C2 at *ca.* 2.4 V) and low-order LiPS (C1 at *ca.* 2.0 V), and one anodic peak for the reverse oxidation process (A1 at *ca.* 2.5 V). Upon closer inspection of the reference cell's CV profile, a third, subtle cathodic shoulder can be observed at a potential slightly below the main C1 peak (*ca.* 1.8–1.9 V). This feature is often attributed to the sluggish kinetics of the final conversion steps in the absence of an effective catalyst. Specifically, it can represent the slow, multi-step electrochemical reduction of short-chain polysulfides (*e.g.*, Li_2S_4 or Li_2S_2) into the final solid products, Li_2S_2 and Li_2S. In contrast, the cell with the CuP_2 interlayer exhibits a more singular and intensified C1 peak, indicating that the catalyst effectively accelerates and merges these final, kinetically challenging reduction steps into a single, more efficient process.

Compared to the reference cell, the cell with CuP_2 interlayer exhibits significantly enhanced redox currents and a lower potential gap between the oxidation and reduction peaks. Specifically, the intensified C1 and C2 peaks indicate that CuP_2 effectively catalyzes the conversion of both long-chain and short-chain LiPS. Furthermore, the A1 oxidation peak shifts cathodically from 2.5 V to 2.4 V, corresponding to a reduction in the Li_2S oxidation overpotential of approximately 100 mV. These CV results collectively demonstrate the superior catalytic activity of CuP_2 for accelerating LiPS redox kinetics.

The enhanced kinetics observed in the CV analysis translate directly to improved galvanostatic performance, as shown in

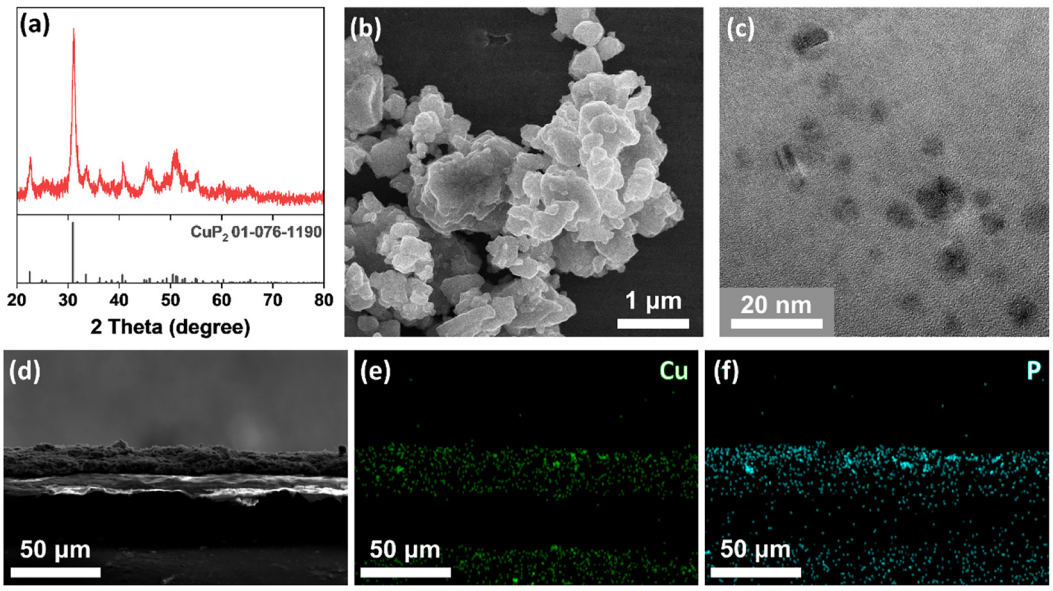

Fig. 1 (a) X-ray diffraction pattern, (b) SEM image, and (c) TEM image of the synthesized CuP_2 powder. (d) Cross-sectional SEM image of the CuP_2-coated separator, and its corresponding (e) Cu and (f) P elemental mapping images.

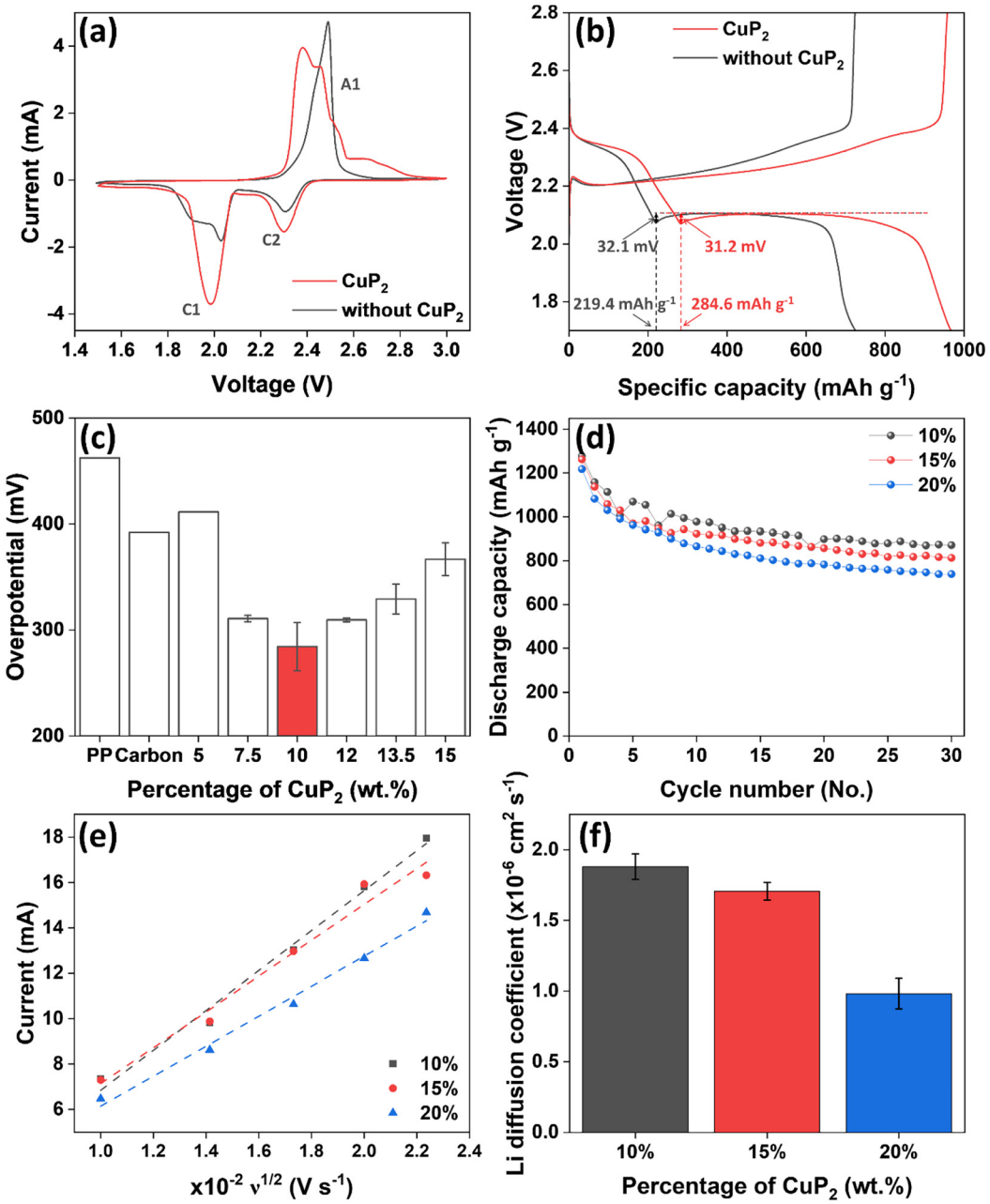

Fig. 2 (a) CV cycles and (b) initial voltage profiles of the cells with and without the CuP_2 interlayer. (c) Overpotential for Li_2S oxidation, as measured by the initial spike during the charging processes for various mixing ratios of CuP_2 at the interlayer. (d) Cycle performance results for the cells containing CuP_2 interlayers. (e) Linear fitting of the cathodic peak currents *versus* the square root of the scan rate for cells, and (f) Li diffusion coefficient (with standard errors) with different CuP_2 mixing ratios (10, 15, and 20%).

the initial charge–discharge profiles (Fig. 2b). The cell with the CuP_2 interlayer delivered a significantly higher initial discharge capacity of 964 mAh g^{-1}, compared to 722.7 mAh g^{-1} for the reference cell. A detailed analysis of the discharge plateaus reveals that CuP_2 enhances sulfur utilization in both conversion steps. The capacity contribution from the upper plateau (2.4–2.1 V, $S_8 \rightarrow Li_2S_4$) increased from 219.4 to 284.6 mAh g^{-1}, while the contribution from the lower plateau (<2.1 V, $Li_2S_4 \rightarrow Li_2S$) increased from 503.3 to 679.4 mAh g^{-1}. The substantial capacity enhancement is consistent with the intensified redox peaks observed in the CV curves, confirming a more complete and efficient sulfur conversion process in the presence of the CuP_2 catalyst.

A critical factor for the long-term cyclability of LSB is the efficient oxidation of solid Li_2S back to soluble LiPS during charging, which can be assessed by the initial charging overpotential. While CuP_2 provides catalytic sites, its conductivity is lower than that of carbon, necessitating an optimization of the

CuP_2 content in the interlayer. As shown in Fig. 2c, the Li_2S oxidation overpotential was systematically evaluated for various CuP_2 weight percentages. A clear trend was observed, with the 10 wt% CuP_2 interlayer exhibiting the lowest overpotential, significantly lower than both the bare separator and the carbon-only interlayer. The underlying mechanism for this trend can be attributed to a critical trade-off between the interlayer's catalytic activity and its overall conductivity (both electronic and ionic). As the CuP_2 content increases from 0 to 10 wt%, the density of catalytically active sites for polysulfide conversion increases, which directly accelerates the redox kinetics and lowers the overpotentials. However, beyond this optimal loading, two detrimental effects begin to dominate. Firstly, since CuP_2 possesses lower electronic conductivity than the carbon matrix, increasing its mass fraction raises the interlayer's overall electrical resistance, impeding efficient electron transfer. Secondly, an excessive amount of CuP_2 nanoparticles can agglomerate and block the pores within the carbon framework, increasing the tortuosity for Li^+ transport through the electrolyte. This hindered ionic conductivity also contributes to a higher overpotential. Therefore, the 10 wt% concentration represents the optimal balance, maximizing catalytic benefits without significantly compromising the essential electronic and ionic pathways required for high performance.

This minimized polarization is directly correlated with improved cycling performance (Fig. 2d), where the cell with 10 wt% CuP_2 also demonstrated the highest capacity retention over 30 cycles. This correlation confirms that rapid Li_2S conversion kinetics, enabled by the optimized catalyst loading, are crucial for enhancing electrochemical performance.

To further quantify the enhanced redox kinetics, CV measurements were performed at various scan rates (0.1–0.5 mV s^{-1}). The relationship between the cathodic peak current and the square root of the scan rate ($\nu^{1/2}$) is plotted in Fig. 2e. For all CuP_2 percentages, the peak currents show a strong linear dependence on $\nu^{1/2}$, indicating that the polysulfide conversion is a diffusion-controlled process. From the slopes of the linear fits in Fig. 2e, the Li-ion diffusion coefficients (D_{Li^+}) were calculated using the Randles–Sevcik equation to provide a more direct quantitative measure of the kinetic behavior.[36] The results are plotted in Fig. 2f. The analysis reveals that the 10 wt% CuP_2 interlayer possesses the highest D_{Li^+} of 1.88×10^{-6} cm^2 s^{-1}, while the diffusivity decreases for the 15% and 20% to 1.71×10^{-6} and 0.98×10^{-6} cm^2 s^{-1}, respectively. The trend strongly suggests that at higher catalyst loadings beyond the 10 wt% optimum, the increased partial blockage of ion transport channels by the CuP_2 nanoparticles begins to hinder the overall Li-ion diffusion kinetics. This quantitative finding is in excellent agreement with our overpotential and cycling data, confirming that the 10 wt% interlayer provides the ideal balance between catalytic activity and efficient mass transport.

To validate the practical benefits of the optimized interlayer, the long-term cycling stability and rate capability were evaluated at 0.2 C, with other reference cycles (CuC_2O_4, P-VS_2@PP, PSN-MXene@2C, MoS_2) shown in Fig. 3.[30,37–39] The cell incorporating the 10 wt% CuP_2 interlayer demonstrated exceptional cycling stability over 500 cycles at a rate of 0.5 C. It maintained a high reversible capacity of 600 mAh g^{-1} at the end of the test, showcasing its robust durability. In stark contrast, the reference cell without the catalyst suffered from rapid capacity degradation, retaining only 200 mAh g^{-1} over a much shorter cycle life. Furthermore, the rate performance of the CuP_2-containing cell was consistently superior to that of the reference cell across all tested current densities, from 0.05 C to 0.5 C (Fig. 3, inset). The enhanced capacity, particularly at higher C-rates, underscores the crucial role of the CuP_2 catalyst in accelerating LiPS redox kinetics and improving overall sulfur utilization.

To elucidate the mechanism behind the enhanced electrochemical performance, the interaction between the CuP_2 catalyst and LiPS was investigated. The strong affinity of CuP_2 for LiPS was first demonstrated through a visual adsorption experiment, as shown in Fig. 4a. Upon adding the black CuP_2 powder to a characteristic yellow Li_2S_6 solution, the solution became completely clear and colorless within three minutes

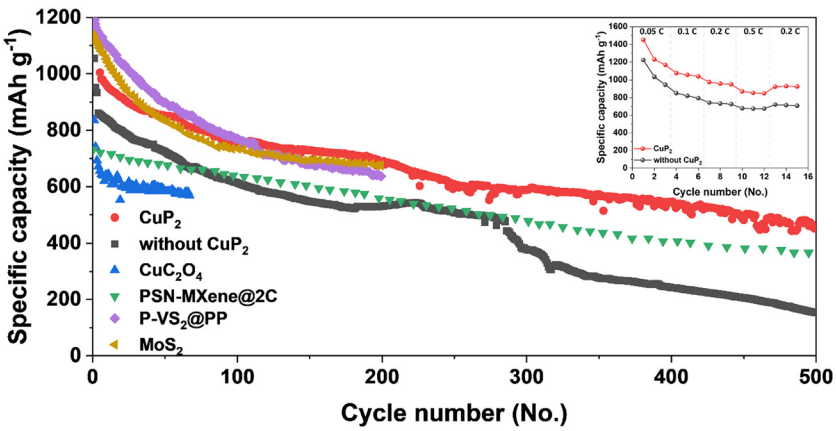

Fig. 3 Long-term cycling performance of the coin half-cells containing a carbon-coated separator both with and without a 10 wt% CuP_2 interlayer, and various references (CuC_2O_4, P-VS_2@PP, PSN-MXene, MoS_2), and C-rate performance (Inset figure).

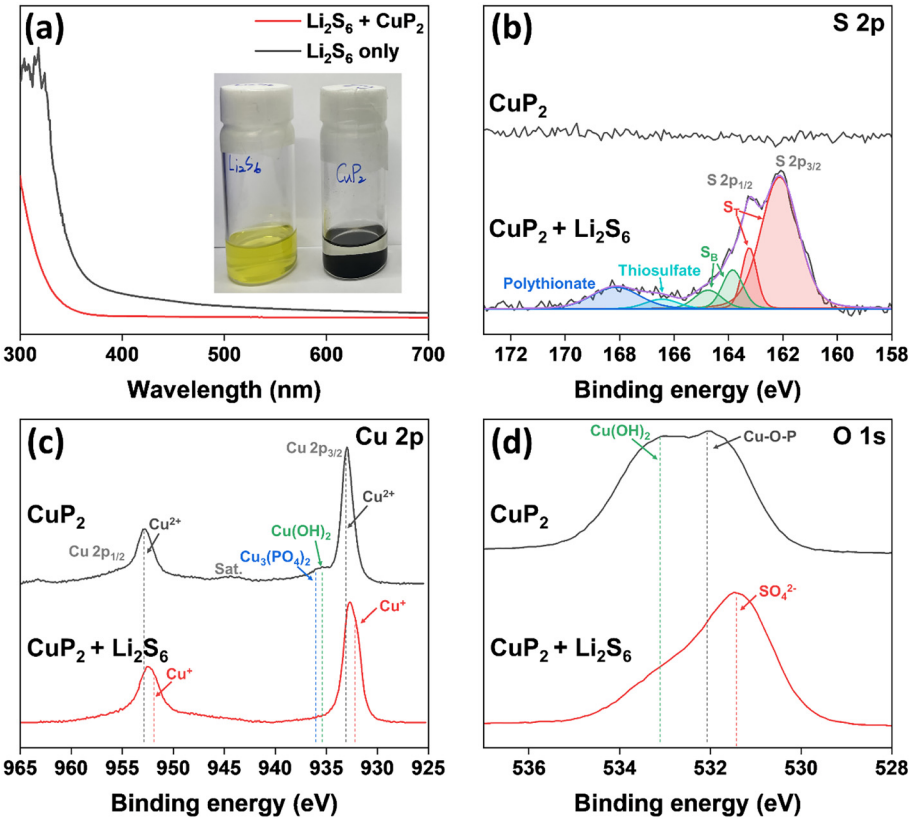

Fig. 4 Changes observed in the (a) UV-vis spectra, and in the (b) S 2p, (c) Cu 2p, and (d) O 1s XPS spectra before and after LiPSs adsorption on the CuP_2 electrocatalyst surface.

(Fig. 4a, inset). This rapid visual change indicates a strong interaction. This observation was quantified by UV-vis spectroscopy, where the spectrum of the supernatant after the addition of CuP_2 showed a near-complete disappearance of the absorbance peaks associated with Li_2S_6. Together, these results provide direct evidence of the rapid and effective adsorption of soluble polysulfides on the CuP_2 surface, which is the crucial first step in anchoring these species and mitigating the shuttle effect.

Following LiPS adsorption, the CuP_2 powder was analyzed by XPS to determine the chemical structure of the LiPS present on the surface of the catalyst. As shown in Fig. 4b, significant changes were observed in the S 2p spectrum after LiPS adsorption, showing no detectable S 2p peaks in the as-prepared CuP_2 powder but emerging peaks in the 162–168 eV range after adsorption. A peak corresponding to bridging sulfur (S_B), which typically represents an –S–S– bond, appeared at 164 eV. In comparison, a peak corresponding to terminal sulfur (S_T) was observed at lower binding energies (<164 eV).[35] Peak deconvolution showed that the S_T peak intensity was approximately twice that of the S_B peak, suggesting that S_T exists in the form of Li–S– or Cu–S– bonds.[40–42] Moreover, peaks were observed corresponding to adsorbed thiosulfate and polythionate species (>166 eV), which are known to be formed on oxygen-rich surfaces. Interestingly, the Cu 2p spectrum also exhibited a key change after LiPS adsorption, as shown in Fig. 4c. In this case, peaks corresponding to Cu^{2+} were initially observed at 932.98 eV (Cu $2p_{3/2}$) and 952.58 eV (Cu $2p_{1/2}$) for the as-prepared CuP_2 surface, along with small amounts of oxides that were generated upon exposure to air (*i.e.*, $Cu_3(PO_4)_2$ at 935.85 eV, and $Cu(OH)_2$ at 934.67 eV).[35,43] However, following the LiPS adsorption experiments, additional Cu^+ peaks were clearly identified at lower binding energies than the main Cu^{2+} peak (*i.e.*, 931.98 eV for Cu $2p_{3/2}$ and 951.73 eV for Cu $2p_{1/2}$). Furthermore, the intensities of the peaks corresponding to $Cu_3(PO_4)_2$ and $Cu(OH)_2$ were reduced. Additionally, a clear difference was observed in the O 1s spectrum after LiPS adsorption. As shown in Fig. 4d, for the as-prepared CuP_2, peaks corresponding to $Cu(OH)_2$ and Cu–O–P (phosphate, $Cu_3(PO_4)_2$) species were observed at 533.08 and 532.08 eV, respectively, which were also attributed to air exposure, consistent with the Cu 2p spectra (Fig. 4c). However, following LiPS adsorption, the $Cu(OH)_2$ and Cu–O–P peak intensities decreased, and a new sulfate peak was observed, indicating that the sulfur atoms of the LiPSs participated in the adsorption process, bonding with the oxygen atoms present on the oxidized surface. These results are consistent with the reduced $Cu_3(PO_4)_2$ and $Cu(OH)_2$ signal intensities observed in Fig. 4c. The XPS results therefore suggest that CuP_2 possesses two adsorption sites, namely the metallic Cu and oxidized Cu surfaces.

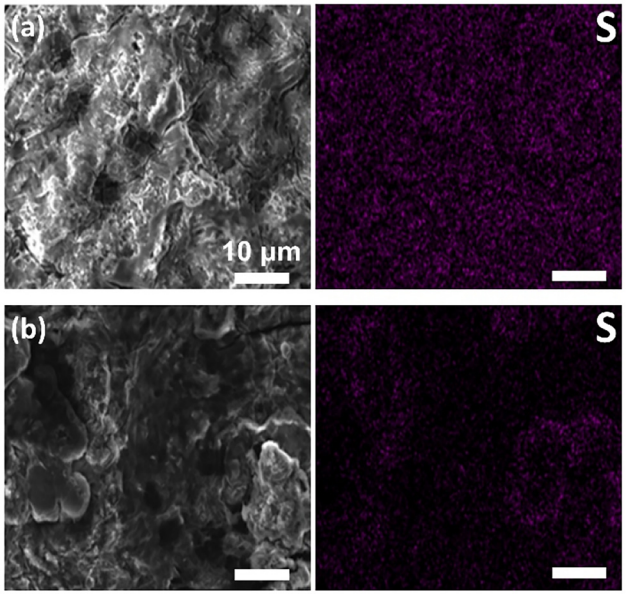

Fig. 5 SEM and EDS mapping images of S on the Li metal surface after the 500-cycle test, (a) without and (b) with the CuP_2 interlayer. All scale bars correspond to 10 μm.

As shown in Fig. 5, sulfur elemental mapping revealed that after 500 charge/discharge cycles, the CuP_2 interlayer reduced sulfur deposition on the lithium surface compared to the system containing no CuP_2 interlayer. In accordance with the proposed mechanism of CuP_2 interaction with the LiPS species, it appears that the interlayer enhances the long-term cycling performance and degree of sulfur utilization by mitigating LiPS shuttling toward the Li metal.

To further validate the electrocatalytic ability of CuP_2, the cycling performances of LSB pouch cells were tested, as shown in Fig. 6. The areal loading of the sulfur-active material was 3 mg cm^{-2}, and the cathode area covered by the CuP_2 interlayer was 15 cm^2. As displayed in Fig. 6a, a different pattern of cycle performance was shown. In the case of the pouch cell containing a conventional sulfur cathode, an increase in capacity was observed within the initial 14 cycles. However, the cathode incorporating the CuP_2 interlayer required a longer time to stabilize the specific capacity curve up to 45 cycles. The phenomenon has its origins in the wetting issues in the porous cathode matrix. The cathode structure incorporating the CuP_2 interlayer has more porous and active sites to accommodate liquid phase LiPS and electrolytes than the conventional cathode structure. It has been demonstrated that CuP_2 interlayer functioned as a reservoir of LiPS, thereby resulting in an increase in capacity retention rate is enhanced due to the porous and electrochemically active structure of the materials. This enhancement in capacity retention is accompanied by the stabilization of performance, as illustrated in Fig. 6b. The pouch cell, which incorporates the CuP_2 interlayer, exhibits a capacity retention of 92% of its initial capacity. In contrast, the conventional pouch cell demonstrates a

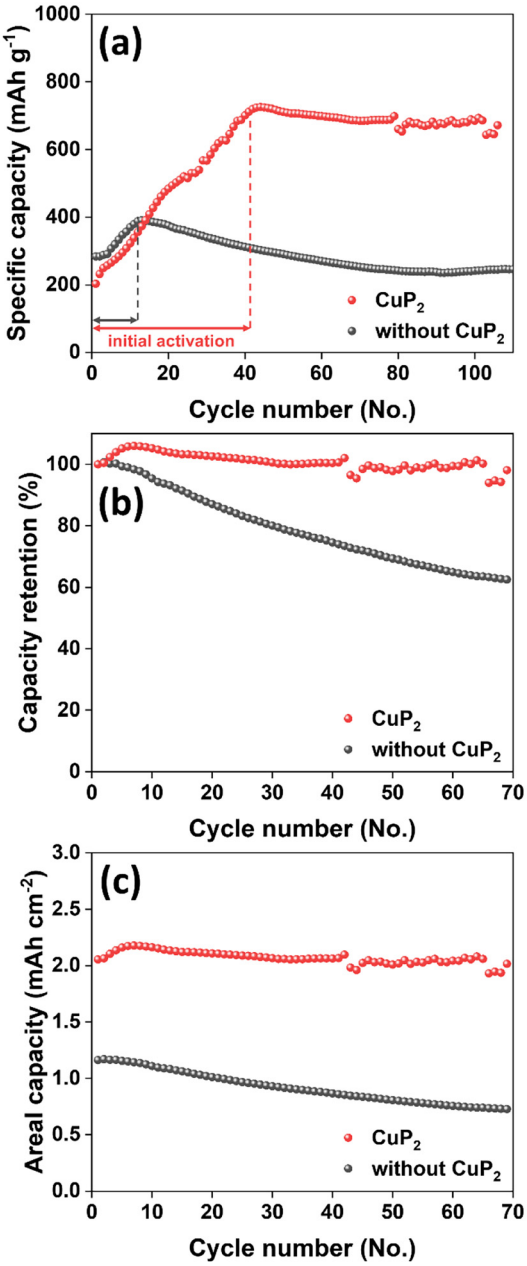

Fig. 6 (a) Specific capacity *vs.* cycle number for the pouch cell, illustrating the initial activation phase followed by stable cycling. To clearly represent the cell's practical and steady performance, the corresponding (b) capacity retention rate and (c) areal capacity are plotted for the cycles following this initial activation. The areal capacity in (c) is calculated from the stabilized specific capacity shown in (a) (*e.g.*, ~730 mAh g^{-1} × 3 mg cm^{-2} ≈ 2.2 mAh cm^{-2}). The tests were run at 0.1 C (1 C = 1672 mA g^{-1}) for the cathodes prepared without and with the CuP_2 interlayer. The cut-off voltage was 1.9–2.6 V, and the areal sulfur loading was 3 mg cm^{-2}.

gradual degradation, reaching a capacity of less than 60% of its initial capacity.

Notably, compared to the pouch cell containing a conventional sulfur cathode, the cathode incorporating the CuP_2 interlayer exhibited twice the areal capacity (2.2 mAh cm^{-2},

726.1 mAh g^{-1}) as shown in Fig. 6c. This result indicates that the CuP_2 interlayer enhances the electrochemical utilization rate of sulfur owing to the strong interactions between the CuP_2 surface and the LiPS species, which ensure a greater availability of active sulfur species in the pouch cell. These findings indicate that electrocatalysts, which are commonly employed for reactions involving oxygen-rich species, such as the oxygen evolution, oxygen reduction, and CO_2 reduction reactions, are well-suited for use in practical LSB applications.

4. Conclusions

In conclusion, this study successfully addresses the critical challenge of long-term stability in lithium–sulfur batteries (LSBs) by introducing a highly effective CuP_2 electrocatalyst, a material previously explored in CO_2 reduction. By incorporating CuP_2 nanoparticles into the interlayer, we achieved a high initial specific capacity of 964 mAh g^{-1} and, more importantly, retained an impressive capacity of 600 mAh g^{-1} after 500 cycles at 0.5 C. The exceptional performance is attributed to the dual-functional nature of the CuP_2 surface, which provides strong polysulfide chemisorption while simultaneously accelerating redox kinetics. Our analysis identified two distinct active sites responsible for this: (i) Cu^{2+} ions that act as redox mediators for terminal sulfur atoms, and (ii) an oxidized phosphide surface that reversibly binds polysulfides as thiosulfate and polythionate. This work validates a new catalyst due to the fundamental analogy between the two elements. This approach of cross-system catalyst discovery opens a promising new avenue for the rational design of high-performance electrocatalysts for next-generation LSBs. Future work incorporating theoretical calculations, such as density functional theory, could further elucidate the atomic-level interactions and reaction pathways, providing a deeper mechanistic understanding.

Conflicts of interest

There are no conflicts to declare.

Data availability

All the data used are included in the manuscript; if raw data is needed, it will be provided upon request to the corresponding author.

Acknowledgements

This work was supported by the National Research Foundation of Korea (NRF) grant funded by the Korea government (MSIT) (NRF-2021K1A4A8A01079455) and the InnoCORE program of the Ministry of Science and ICT (1.260005.01).

References

1 A. G. Olabi and M. A. Abdelkareem, *Renewable Sustainable Energy Rev.*, 2022, **158**, 112111.
2 A. Gupta and A. Manthiram, *Adv. Energy Mater.*, 2020, **10**, 2001972.
3 J. Hassoun and B. Scrosati, *Angew. Chem., Int. Ed.*, 2010, **49**, 2371–2374.
4 M. Wild, L. O'Neill, T. Zhang, R. Purkayastha, G. Minton, M. Marinescu and G. J. Offer, *Energy Environ. Sci.*, 2015, **8**, 3477–3494.
5 J. Choi, J. D. Pascasio and J. Lee, *Dalton Trans.*, 2025, **54**, 9754–9760.
6 J. Park, H. Yoo and J. Choi, *J. Power Sources*, 2019, **431**, 25–30.
7 C. Lee, J. W. Kim and J. Lee, *Dalton Trans.*, 2024, **53**, 6575–6582.
8 Y. Yan, L. Wei, X. Su, S. Deng, J. Feng, J. Yang, M. Chi, H. Lei, Z. Li and M. Wu, *ChemNanoMat*, 2020, **6**, 274–279.
9 D. N. Fronczek and W. G. Bessler, *J. Power Sources*, 2013, **244**, 183–188.
10 Y. Diao, K. Xie, S. Xiong and X. Hong, *J. Power Sources*, 2013, **235**, 181–186.
11 H. Zhao, N. Deng, J. Yan, W. Kang, J. Ju, Y. Ruan, X. Wang, X. Zhuang, Q. Li and B. Cheng, *Chem. Eng. J.*, 2018, **347**, 343–365.
12 N. Pal and A. J. Bhattacharyya, *J. Phys. Chem. C*, 2023, **127**, 5713–5719.
13 H. Wang, Y. Yang, Y. Liang, J. T. Robinson, Y. Li, A. Jackson, Y. Cui and H. Dai, *Nano Lett.*, 2011, **11**, 2644–2647.
14 X. Feng, M.-K. Song, W. C. Stolte, D. Gardenghi, D. Zhang, X. Sun, J. Zhu, E. J. Cairns and J. Guo, *Phys. Chem. Chem. Phys.*, 2014, **16**, 16931–16940.
15 L. Zhang, L. Ji, P.-A. Glans, Y. Zhang, J. Zhu and J. Guo, *Phys. Chem. Chem. Phys.*, 2012, **14**, 13670–13675.
16 S. Moon, Y. H. Jung, W. K. Jung, D. S. Jung, J. W. Choi and D. K. Kim, *Adv. Mater.*, 2013, **25**, 6547–6553.
17 D.-W. Wang, Q. Zeng, G. Zhou, L. Yin, F. Li, H.-M. Cheng, I. R. Gentle and G. Q. M. Lu, *J. Mater. Chem. A*, 2013, **1**, 9382–9394.
18 H. Li, X. Wen, F. Shao, C. Zhou, Y. Zhang, N. Hu and H. Wei, *Chem. Eng. J.*, 2021, **412**, 128562.
19 Y.-T. Liu, S. Liu, G.-R. Li, T.-Y. Yan and X.-P. Gao, *Adv. Sci.*, 2020, **7**, 1903693.
20 Z.-Y. Wang, L. Wang, S. Liu, G.-R. Li and X.-P. Gao, *Adv. Funct. Mater.*, 2019, **29**, 1901051.
21 Y.-W. Song, L. Shen, X.-Y. Li, C.-X. Zhao, J. Zhou, B.-Q. Li, J.-Q. Huang and Q. Zhang, *Nat. Chem. Eng.*, 2024, **1**, 588–596.
22 Z.-X. Chen, J.-J. Zhao, G.-Y. Fang, F. Sun, M. Zhao, X.-Q. Zhang, B.-Q. Li and J.-Q. Huang, *J. Energy Chem.*, 2025, **109**, 129–137.
23 Y.-W. Song, J. Zhou, Z.-X. Chen, J.-D. Zhang, L. Shen, F. Sun, M. Zhao and B.-Q. Li, *J. Energy Chem.*, 2025, **106**, 993–1001.

24 Z.-X. Chen, J.-J. Zhao, G.-Y. Fang, S. Zhang, J. Ma, M. Zhao, B.-Q. Li and J.-Q. Huang, *Energy Storage Mater.*, 2025, **83**, 104502.
25 Z.-W. Zhang, H.-J. Peng, M. Zhao and J.-Q. Huang, *Adv. Funct. Mater.*, 2018, **28**, 1707536.
26 W. Huang, Z. Lin, H. Liu, R. Na, J. Tian and Z. Shan, *J. Mater. Chem. A*, 2018, **6**, 17132–17141.
27 C. Dai, J.-M. Lim, M. Wang, L. Hu, Y. Chen, Z. Chen, H. Chen, S.-J. Bao, B. Shen, Y. Li, G. Henkelman and M. Xu, *Adv. Funct. Mater.*, 2018, **28**, 1704443.
28 J. Park, S. Kim, G. Lee and J. Choi, *ACS Omega*, 2018, **3**, 10205–10210.
29 Y. J. Choi, B. S. Jung, D. J. Lee, J. H. Jeong, K. W. Kim, H. J. Ahn, K. K. Cho and H. B. Gu, *Phys. Scr.*, 2007, **2007**, 62.
30 J. W. Kim, G. Seo, S. Bong and J. Lee, *ChemSusChem*, 2021, **14**, 876–883.
31 G. Liu, Q. Zeng, Z. Fan, S. Tian, X. Li, X. Lv, W. Zhang, K. Tao, E. Xie and Z. Zhang, *Chem. Eng. J.*, 2022, **448**, 137683.
32 H. Yuan, H.-J. Peng, J.-Q. Huang and Q. Zhang, *Adv. Mater. Interfaces*, 2019, **6**, 1802046.
33 C. Qi, M. Cai, Z. Li, J. Jin, B. V. R. Chowdari, C. Chen and Z. Wen, *Chem. Eng. J.*, 2020, **399**, 125674.
34 S. Yang, D. Jiang, Q. Su, S. Yuan, Y. Guo, K. Duan, M. Xiang, J. Guo, W. Bai and S. Chou, *Adv. Energy Mater.*, 2024, **14**, 2400648.
35 M. Choi, S. Bong, J. W. Kim and J. Lee, *ACS Energy Lett.*, 2021, **6**, 2090–2095.
36 J. D. Pascasio, M. Park, S. Bae, J. Choi, J. Kim and J. Lee, *J. Power Sources*, 2025, **647**, 237326.
37 G. Liu, Q. Zeng, Z. Fan, S. Tian, X. Li, X. Lv, W. Zhang, K. Tao, E. Xie and Z. Zhang, *Chem. Eng. J.*, 2022, **448**, 137683.
38 Z.-H. Luo, M. Zheng, M.-X. Zhou, X.-T. Sheng, X.-L. Chen, J.-J. Shao, T.-S. Wang and G. Zhou, *Adv. Mater.*, 2025, **37**, 2417321.
39 M. Zheng, C. Guo, Z. Luo, J. Wu, X. Tang, L. Li, Q. Sun, Q. Ouyang, B. Shi, H. Nie, J.-J. Shao and G. Zhou, *Composites, Part B*, 2023, **264**, 110898.
40 X. Liang, C. Y. Kwok, F. Lodi-Marzano, Q. Pang, M. Cuisinier, H. Huang, C. J. Hart, D. Houtarde, K. Kaup, H. Sommer, T. Brezesinski, J. Janek and L. F. Nazar, *Adv. Energy Mater.*, 2016, **6**, 1501636.
41 Q. Pang, D. Kundu, M. Cuisinier and L. F. Nazar, *Nat. Commun.*, 2014, **5**, 4759.
42 M. J. Lacey, A. Yalamanchili, J. Maibach, C. Tengstedt, K. Edström and D. Brandell, *RSC Adv.*, 2016, **6**, 3632–3641.
43 J. Park, S. Bae, J.-S. Park, S. Bong and J. Lee, *ACS Appl. Nano Mater.*, 2021, **4**, 8145–8153.